OPEN ACCESS
IOP Publishing
Journal of Physics: Condensed Matter
J. Phys.: Condens. Matter **32** (2020) 165702 (7pp)
https://doi.org/10.1088/1361-648X/ab6868

Anomalous lattice stiffening in tungsten tetraboride solid solutions with manganese under compression

Haijing Li[1,2], Qiang Tao[3], Juncai Dong[1,2,4,5], Yu Gong[1], Zhiying Guo[1], Jiangwen Liao[1], Xinyu Hao[1], Pinwen Zhu[3], Jing Liu[1] and Dongliang Chen[1,2,5]

[1] Beijing Synchrotron Radiation Facility, Institute of High Energy Physics, Chinese Academy of Sciences, Beijing 100049, People's Republic of China
[2] University of Chinese Academy of Sciences, Beijing 100049, People's Republic of China
[3] State Key Laboratory of Superhard Materials, College of Physics, Jilin University, Changchun 130012, People's Republic of China
[4] Department of Chemistry and Biochemistry, University of California, Los Angeles, CA 90095, United States of America

E-mail: dongjc@ihep.ac.cn and chendl@ihep.ac.cn

Received 26 August 2019, revised 11 December 2019
Accepted for publication 7 January 2020
Published 23 January 2020

Abstract

Tungsten tetraboride (WB_4)-based solid solutions represent one of the most promising superhard metal candidates; however, their underlying hardening mechanisms have not yet been fully understood. Here, we explore the lattice compressibility of WB_4 binary solid solutions with different manganese (Mn) concentrations using high-pressure x-ray diffraction (XRD) up to 52 GPa. Under initial compression, the lattices of low and high Mn-doped WB_4 alloys (i.e. $W_{0.96}Mn_{0.04}B_4$ and $W_{0.84}Mn_{0.16}B_4$) are shown to be more and less compressible than pure WB_4, respectively. Then, a *c*-axis softening is found to occur above 39 GPa in WB_4, consistent with previous results. However, an anomalous sudden *a*-axis stiffening is revealed at ~36 GPa in $W_{0.96}Mn_{0.04}B_4$, along with suppression of *c*-axis softening observed in WB_4. Furthermore, upon Mn addition, a simultaneous stiffening of *a*- and *c*-axes is demonstrated in $W_{0.84}Mn_{0.16}B_4$ at ~37 GPa. Speculation on the possible relationship between this anomalous stiffening and the combined effects of valence-electron concentration (VEC) and atomic size mismatch is also included to understand the origin of the nearly identical hardness enhancement in those two solid solutions compared to WB_4. Our findings emphasize the importance of accurate bonding and structure manipulation via solute atoms to best optimize the hardness of WB_4 solid solutions.

Keywords: superhard, WB_4, solid solution, lattice compressibility, high pressure, XRD

Supplementary material for this article is available online

(Some figures may appear in colour only in the online journal)

[5] Author to whom any correspondence should be addressed.

1. Introduction

The development of superhard materials based on transition metal (TM) borides has recently attracted a great deal of attention due to potential applications in cutting and forming tools and wear-resistant coatings [1–3]. With a flexibility to simultaneously optimize covalent bonding and valence-electron density, TM borides exhibit not only a wide range of mechanical, thermal and electronic properties, but also a variety of crystal lattices with different connectivity of boron atoms ranging from isolated borons to boron networks to a boron skeleton [1–8]. Among these, the highest boride of tungsten, i.e. tungsten tetraboride (WB_4), is of specific interest because of its extremely high Vickers hardness of ~43 GPa (0.49 N applied load), high bulk modulus of 326–339 GPa, high differential stress of up to ~19.7 GPa and lower cost constitutes as compared with other borides (e.g. ReB_2, OsB_2) [9–12]. Moreover, the hardness of WB_4 can be dramatically enhanced via solid solution and extrinsic effects such as second phase and morphology change [13–17]. The maximum low-load hardness values obtained for various WB_4 alloys are summarized in supporting information table 1 (stacks.iop.org/JPhysCM/32/165702/mmedia). Particularly for the intrinsic solid solution hardening, TM dopants of varying valence electron count and atomic size can be incorporated into WB_4 lattice owing to its unique defective cubic dodecaboride structure, which had caused several unusual hardening behaviors [17, 18]. For instance, all the optimized Vickers hardness values in WB_4 binary solid solutions were achieved at rather low content of the dopants, e.g. 2.0 at. % for Ta, 4.0 at. % for Mn and 10.0 at. % for Cr. Besides, two nearly equivalent hardness values were observed in WB_4 solid solutions with 4.0 and 10.0 at. % Mn, suggesting that multiple hardening mechanisms are at work. Further hardness increase was obtained in ternary solid solutions (e.g. $W_{0.94}Ta_{0.02}Mn_{0.04}B_4$ and $W_{0.93}Ta_{0.02}Cr_{0.05}B_4$). Therefore, a full understanding of the underlying mechanisms for those hardness enhancements observed in WB_4-based solid solutions is crucial to guide the design of new superhard borides.

Superhard materials generally possess a high bulk modulus, high shear modulus and a high shear strength [19]; thus, high-pressure studies were used to explore the lattice compressibility and lattice-supported differential stress (a lower-bound estimate of compressive yield strength) in WB_4 solid solutions [10, 11, 17, 18, 20–23]. In pure WB_4, by using high-pressure x-ray diffraction (XRD), Xie *et al* found a more compressible *a*-axis than the *c*-axis up to 42 GPa and then a discontinuous change in the slope of *c*/*a* ratio at ~42 GPa caused by sudden softening of *c*-axis [11]. They proposed it to be a reversible second-order phase transition owing to the rigid structure of WB_4. Then, the same authors performed a comprehensive radial XRD study on WB_4 and WB_4 solid solutions under non-hydrostatic pressure [10, 18]. By comparing the lattice-supported differential stress, they attempted to distinguish between various hardening mechanisms such as electronic structure effect, atomic-size mismatch effect and extrinsic effects. However, except for the ternary solid solution $W_{0.93}Ta_{0.02}Cr_{0.05}B_4$ [17], the lattice compressibility of other WB_4 binary solid solutions can hardly be found in the literature and thus remains unknown yet. Actually, several counterintuitive phenomena had already been demonstrated in $W_{0.93}Ta_{0.02}Cr_{0.05}B_4$ [17]. Specifically, this compound showed an abnormal small increase in bulk modulus based on the second-order fits as compared to WB_4, which contrasts the Vegard's law for solid solutions as neither Ta nor Cr borides are predicted to be stiffer than WB_4. In addition, $W_{0.93}Ta_{0.02}Cr_{0.05}B_4$ was less compressible in the *a*-axis than it is along the *c*-axis and showed no signs of lattice instability, indicating a complete suppression of the pressure-induced phase transition observed in pure WB_4. Those results raise several critical questions: (1) How can the TMs with different atomic size and valence electron count affect the anisotropy of lattice compression and the lattice instability in WB_4-based binary solid solutions? (2) How would the lattice deformation behaviors evolve with TMs concentration?

In this work, we performed synchrotron-based XRD experiments using a diamond anvil cell (DAC) to evaluate the anisotropy of the lattice deformation behaviors and compressibility in WB_4 solid solutions with low and high Mn concentrations. We specifically examined the TM element of Mn, because of the much smaller atomic radius of Mn (Mn = 1.32 Å) than tungsten (W = 1.41 Å; note B = 0.78 Å), the larger valence electron counts of Mn (Mn, Group VII) than tungsten (W Group VI), and the unusual two hardness maxima observed in low and high Mn-doped WB_4 [17]. A parallel set of experiments were also performed on pure WB_4, which allows us to make a comparison of the lattice behaviors as objective as possible. We surprisingly find a successive stiffening of the *a*- and *c*-axes in low and high Mn-doped WB_4 alloys, which contrasts prominently to pure WB_4. Those findings point out to the significance of accurate manipulation of valence-electron concentration (VEC) and atomic size mismatch via solute atoms to best optimize the hardness of WB_4-based solid solutions.

2. Experiments procedure

WB_4 alloys with Mn were synthesized from the pure elements using hot pressing similar to our previously reported method [24]. Specifically, high-purity powders of tungsten (99.95% in purity), manganese (99.99% in purity) and amorphous boron (99.99%) at desired set of compositions (WB_4, $W_{0.96}Mn_{0.04}B_4$ and $W_{0.84}Mn_{0.16}B_4$) were first ground together thoroughly in an agate mortar and pestle to obtain homogeneous mixtures. Then, the mixed powders were cold-pressed into cylindrical samples of 4 mm in diameter and 3 mm in height. Finally, the samples were carried out in a cubic anvil HPHT apparatus (SPD-6 × 600) at a temperature of 2300 K and a pressure of 5.2 GPa for a holding time of 15 min. The as-synthesized ingots were cut into halves for further analysis. One half was crushed into a fine sub-40 μm powder and used to confirm the phase purity by XRD. The XRD patterns were collected on a Bruker D8-Advanced x-ray diffractometer using Cu K_α radiation, with a scan range of $10° < 2\theta < 100°$. Because of the possible volatility of metal elements, inductively coupled plasma mass

spectrometry (ICP-MS) was used to confirm their concentration in the final samples. The other half samples were polished to an optically flat surface using polishing machine equipped with diamond films of 1600 mesh and emery papers of 800–2000 grit sizes. Then, the polished samples were used for surface characterization by scanning electron microscope (SEM) as well as Vickers hardness measurement using a micro-hardening tester equipped with a pyramid diamond indenter tip. For hardness test, the samples were indented using five different applied loads (i.e. 0.49, 0.98, 1.96, 2.94, 4.9, and 9.6 N) with a dwell time of 15 s.

In-situ high-pressure XRD experiments were carried out at the 4W2 beamline of the Beijing Synchrotron Radiation Facility (BSRF) by angle-dispersive measurements with a wavelength of 0.6199 Å and focused x-ray beam size of 26×8 μm^2 (FWHM). Pressure was generated by a symmetric piston-cylinder type DAC with a pair of diamond anvils having a culet size of 300 μm. A rhenium (Re) gasket pre-indented to 30 μm in thickness with a drilled hole of 110 μm in diameter was used into the chamber with silicone oil as the pressure-transmitting medium. The pressure was determined by ruby fluorescence method. The diffraction patterns of the sample were recorded using a 2D PILATUS detector and integrated using the FIT2D software [25]. Rietveld refinements on high-pressure data were carried out with the GSAS package [26].

3. Results

The phase purity of the as-synthesized WB_4, $W_{0.96}Mn_{0.04}B_4$ and $W_{0.84}Mn_{0.16}B_4$ samples was first examined using XRD. As shown in figure 1(a), the XRD patterns of the samples match very well with the reference data available for pure WB_4 in the JCPDS database [27]. In addition, they have no extra diffraction peaks corresponding to the impurity phases of WB_2 (with major peaks at $2\theta = 25.3°$ and 34.7°) and MnB_4 (with major peaks at $2\theta = 35.1°$ and 47.6°), which is consistent with the reported solubility of Mn in WB_4 (˂20 at. %) [17] and hence confirms the high-quality of the synthesized alloy samples. Interestingly, although Mn (1.32 Å) has a much smaller atomic radius than W (1.41 Å), there is no obvious sign for the shift of the diffraction peaks towards higher 2θ angle direction with increase of Mn concentration (figure 1(a)). Actually, the XRD analysis by Rietveld refinement shows a slight expansion for the lattice parameters of the hexagonal crystal cell ($P6_3/mmc$) with increase of Mn concentration (supporting information table 2 and figure 1). This result is in contrast to the Vegard's law for the atomic size-mismatch alloys [28], implying an anomalous effect of Mn on the lattice behavior of WB_4. The morphology and composition purity was checked by SEM in figure 1(b). There is a coexistence of the metallic phase (gray) and the boron phase [14], but no obvious area and pattern changes are shown for the two phases by tuning Mn concentration. Moreover, the ICP-MS results show that the actual metal proportion of Mn in the two samples are only slightly lower than the nominal proportion because of the possible volatility of metal elements (insets in figure 1(b)), thus confirming the low (⩽5 at. %) and high concentrations (⩾10 at. %) for Mn in WB_4 alloys. In WB_4–Mn solid solutions, Mohammadi *et al* found that the hardness of WB_4 could be tuned by adding different concentration of Mn and the hardness data shows two nearly equivalent peaks with 4.0 and 10.0 at. % Mn addition [17]. From figure 1(c), it can be observed that while the Vickers hardness of WB_4 in this work is in good agreement with previous reported values, the hardness values of $W_{0.96}Mn_{0.04}B_4$ and $W_{0.84}Mn_{0.16}B_4$ samples also coincide well with the two peak values reported by Mohammadi *et al*, verifying the presence of different hardening behaviors at low and high Mn concentrations. Therefore, it is of great necessity to understand the underlying mechanism for these extraordinary hardness increases in WB_4–Mn solid solutions.

Figure 2 shows the pressure-induced evolution of the XRD patterns for WB_4, $W_{0.96}Mn_{0.04}B_4$ and $W_{0.84}Mn_{0.16}B_4$. The pure WB_4 exhibits six diffraction peaks (1 0 1, 0 0 2, 1 1 0, 2 0 1, 1 1 2, 1 0 3), and no evidence of dramatic peak broadening or peak splitting was observed over the entire pressure range (figure 2(a)), which is consistent with previous results [11, 22]. All the Bragg peaks are also well preserved for the two solid solutions under compression, without unusual peak broadening or splitting. Hence, it is reasonable to conclude that, just like WB_4, the two solid solutions also remain in the hexagonal crystal structure up to the highest pressure of ~52 GPa. However, it is noteworthy that the two solid solutions exhibit obviously different pressure dependence as compared to WB_4. For example, with pressure increasing to ~52 GPa, the (1 1 0) peak in WB_4 shows a shift of $\Delta\theta = 0.5°$ toward high angle, as compared to $\Delta\theta = 0.7°$ and 0.3° in $W_{0.96}Mn_{0.04}B_4$ and $W_{0.84}Mn_{0.16}B_4$, respectively. Similar tendency is also illustrated by comparing the pressure evolution of other peaks. These preliminary XRD results have already indicated that the lattice of $W_{0.96}Mn_{0.04}B_4$ may be more compressible than that of WB_4, whereas $W_{0.84}Mn_{0.16}B_4$ can support a higher uncompressible lattice, indicating an anomalous modification of the WB_4 lattice compressibility by different Mn concentration.

Figure 3 shows the normalized unit cell volume as a function of pressure for the solid solution samples, with the best Riveted refinement patterns shown in supporting information figure 2. Because the reported zero-pressure bulk modulus of pure WB_4 was shown to depend critically on the pressure range and the choice of EOS [11, 17], we first investigate the compressibility of the fractional *a*- and *c*-lattice parameters (figure 4) to examine the structural stability in relation to Mn concentration. From figure 4, it can be observed that under initial compression, pure WB_4 is less compressible (i.e. stiffer) in the *c*-axis than it is along the *a*-axis, with both lattice constants showing a smooth decrease up to 39 GPa. However, further compression at ~39 GPa results in a sudden softening of the *c*-axis, which becomes significantly more compressible than the *a*-axis that does not show any change in behavior. These behaviors for WB_4 are in good agreement with previous results by Xie *et al* [11]. However, a number of other extraordinary trends are demonstrated for the $W_{1-x}Mn_xB_4$ solid solutions. In particular, just like WB_4, both $W_{0.96}Mn_{0.04}B_4$ and $W_{0.84}Mn_{0.16}B_4$

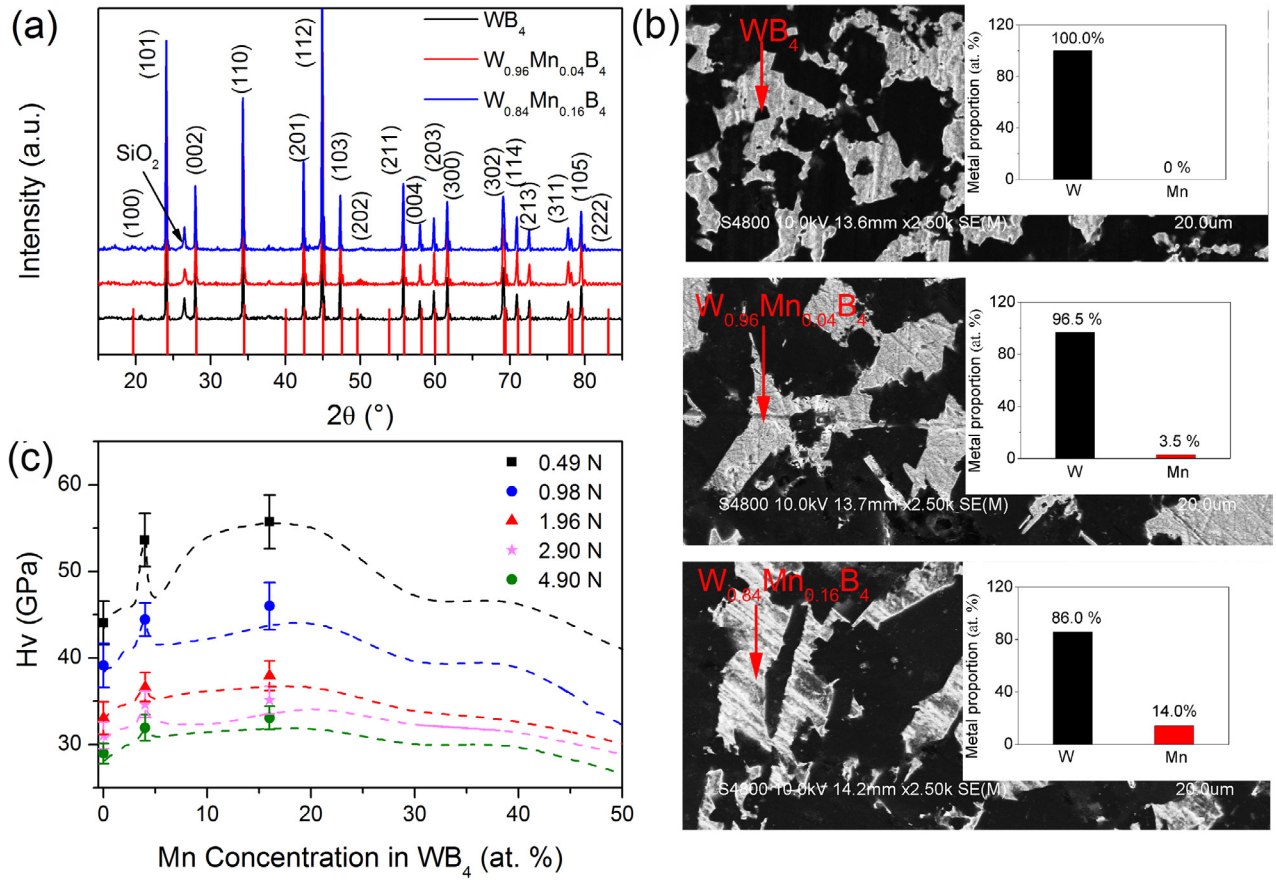

Figure 1. (a) XRD patterns of pure WB_4 and WB_4–Mn solid solutions. The stick pattern given below is from the Joint Committee on Powder Diffraction Standards (JCPDS 00-019-1373) for pure WB_4. The peak ($2\theta = 26.5°$) of SiO_2 results from the agate mortar used to ground the samples. (b) Surface SEM images of the alloys. While black areas correspond to boron, gray areas correspond to metallic phases. The insets show the actual metal proportion of W and Mn in doped samples on a metals basis obtained by ICP-MS. (c) Vickers micro-indentation hardness of the alloys under different loads (solid data points). The previously reported hardness values [17] are added for comparison (dashed lines).

show a linear decrease in the *a*- and *c*-lattice constants up to a pressure of ~36 GPa, with the *a*-axis being the most compressible one; nevertheless, $W_{0.96}Mn_{0.04}B_4$ is apparently more compressible than WB_4, as compared to the close compressibility between $W_{0.84}Mn_{0.16}B_4$ and WB_4. Besides, the linear compressibility between the *a*- and *c*-axes in $W_{0.96}Mn_{0.04}B_4$ ($\beta_{a\text{-axis}} = 1.32 \times 10^{-3}$ GPa^{-1} and $\beta_{c\text{-axis}} = 1.14 \times 10^{-3}$ GPa^{-1}) and $W_{0.84}Mn_{0.16}B_4$ ($\beta_{a\text{-axis}} = 0.726 \times 10^{-3}$ GPa^{-1} and $\beta_{c\text{-axis}} = 0.658 \times 10^{-3}$ GPa^{-1}) appears to be much more similar than that of pure WB_4 ($\beta_{a\text{-axis}} = 0.882 \times 10^{-3}$ GPa^{-1} and $\beta_{c\text{-axis}} = 0.701 \times 10^{-3}$ GPa^{-1}), indicating the creation of a much more isotropic bonding after the addition of Mn in WB_4. This result agrees well with the general trend that isotropic structures favor high hardness [11]. Most interestingly, as the pressure increases above 36 GPa, the *c*-axis in $W_{0.96}Mn_{0.04}B_4$ continues to have a smooth decrease, whereas the *a*-axis appears to undergo a sudden stiffening and becomes obviously less compressible than the *c*-axis. Furthermore, with the increase of Mn concentration in $W_{0.84}Mn_{0.16}B_4$, not only the *a*- but also *c*-axes simultaneously exhibit a tendency for stiffening after 37 GPa and are characterized by comparable compressibility afterwards. Such a strengthening of the *a*- and *c*-axes observed in WB_4–Mn solutions are drastically distinct from the lattice softening in pure WB_4 as well as the swap of the most compressible direction from *a*- to *c*-axis in $W_{0.93}Ta_{0.02}Cr_{0.05}B_4$ alloy [10, 11, 17], suggesting that the addition of Mn can greatly modify the compressibility along different crystallographic axes in hexagonal WB_4.

The trends in bulk modulus change among the solid solution samples are then investigated (figure 3). Because of the extraordinary behaviors in the *a*- and *c*-directions and for a fair comparison with WB_4, fits to the Birch-Murnaghan EOS were performed at pressures before the occurrence of lattice stiffening in WB_4–Mn solid solutions (~36 GPa). For WB_4, we obtain $K_0 = 334 \pm 8$ GPa (second-order Birch–Murnaghan EOS) and $K_0 = 351 \pm 3$ GPa with $K_0' = 1.3 \pm 0.6$ (third-order Birch–Murnaghan EOS) (table 1). Those values are in well accordance with the obtained pairs $(K_0, K_0') = (326 \pm 3, 4)$ and $(369 \pm 9, 1.2 \pm 0.5)$ by Xie *et al* [11]. For $W_{0.96}Mn_{0.04}B_4$, the measured K_0 is 318 ± 7 GPa (second-order Birch–Murnaghan EOS) and 339 ± 2 GPa with $K_0' = 1.5 \pm 0.4$, which is about 4% smaller than that of WB_4. By contrast, the bulk modulus of $W_{0.84}Mn_{0.16}B_4$ is $K_0 = 352 \pm 13$ GPa (second-order Birch–Murnaghan EOS) and $K_0 = 366 \pm 6$ GPa with $K_0' = 2.9 \pm 0.4$, which is approximately 5% larger than that of WB_4. Besides, we note that the measured bulk modulus of

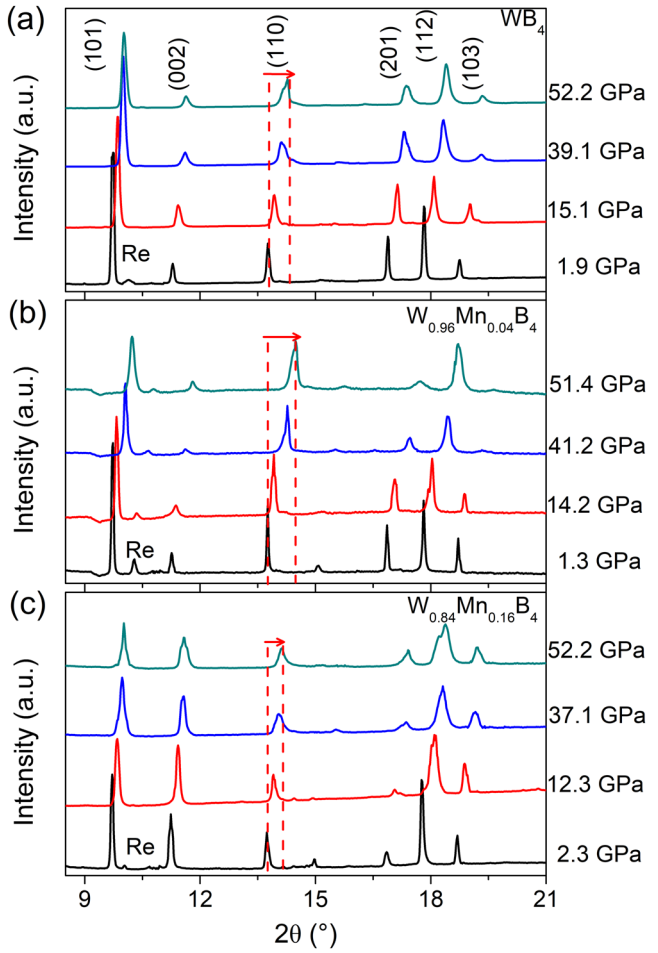

Figure 2. Representative XRD patterns for WB_4, $W_{0.96}Mn_{0.04}B_4$ and $W_{0.84}Mn_{0.16}B_4$ samples as a function of increasing pressure. The Re peaks is from the gasket due to incomplete filtering of the tails of x-ray beam. The red dashed line highlights the movement of the (1 1 0) peak in different samples.

$W_{0.84}Mn_{0.16}B_4$ is similar to the previously reported bulk modulus for the hardest WB_4 solid solution of $W_{0.93}Ta_{0.02}Cr_{0.05}B_4$, having $K_0 = 346 \pm 3$ GPa from the second-order fit and $K_0 = 366 \pm 14$ GPa with $K_0' = 2.6 \pm 0.9$ from the third-order fit over the pressure range of 0–40 GPa [17]. All the obtained values are summarized in table 1. The nonlinear decrease of the bulk modulus in $W_{1-x}Mn_xB_4$ is somewhat surprising, since the bulk modulus usually follows Vegard's law for solid solutions [28] and MnB_4 was reported to have a bulk modulus (250–280 GPa) [29, 30] much smaller than pure WB_4. These extraordinary behaviors in lattice compressibility suggest that different strengthening mechanisms should be at work at different Mn concentrations.

4. Discussion

Just as WB_4, the diffraction patterns of WB_4 alloys with Mn remain the same at the point of structural change at ~36 GPa, and no evidence of dramatic peak broadening or peak splitting is demonstrated. Actually, the full-width at half maxima (FWHM) profiles for the (1 0 1) and (1 1 0) peaks of the samples show a gradual increase with elevated pressure

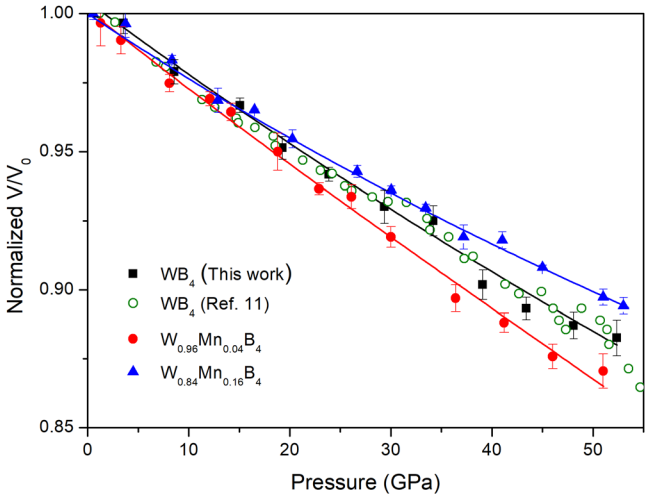

Figure 3. Normalized unit cell volume of WB_4, $W_{0.96}Mn_{0.04}B_4$ and $W_{0.84}Mn_{0.16}B_4$ plotted as a function of pressure. Solid symbols represent this study, and open symbols denote previous studies. All the solid lines are the fits to the Birch–Murnaghan EOS.

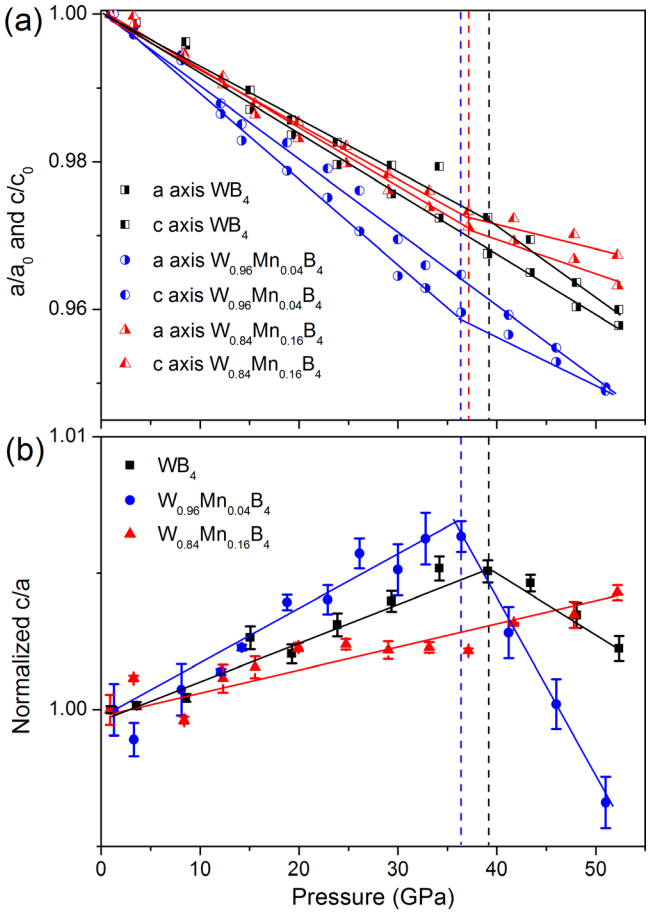

Figure 4. (a) The normalized lattice parameters and (b) *c*/*a* ratio plotted as a function of pressure for the $W_{0.96}Mn_{0.04}B_4$ and $W_{0.84}Mn_{0.16}B_4$ solid solutions as compared to pure WB_4. The dashed lines highlight the discontinuity of the lattice parameter evolution for pure WB_4 (black), $W_{0.96}Mn_{0.04}B_4$ (blue) and $W_{0.84}Mn_{0.16}B_4$ (red).

(supporting information figure 3), which can be related to the reduction of particle size and enhancement of lattice strain [31]. Thus, the possibility of a first-order phase transition can

Table 1. Comparison of the experimental results for the bulk modulus K_0 (GPa) and their first derivative K_0'. Error values are quoted in parentheses.

	WB_4		$W_{0.96}Mn_{0.04}B_4$		$W_{0.84}Mn_{0.16}B_4$	
Pressure (GPa)	K_0 (GPa)	K_0'	K_0 (GPa)	K_0'	K_0 (GPa)	K_0'
39	334 (8)	4	—	—	—	—
	351 (3)	1.3 (6)	—	—	—	—
36	—	—	318 (7)	4	—	—
	—	—	339 (2)	1.5 (4)	—	—
37	—	—	—	—	352 (13)	4
	—	—	—	—	366 (6)	2.9 (4)

be precluded. Additionally, because of the much larger transition pressure for WB_4–Mn solid solutions (~36 GPa) than the hydrostatic limit of the pressure medium (~8 GPa for silicone oil) [32], this observation unlikely results from the deviation from hydrostaticity. Also, the good agreement between our results for WB_4 and previous results by Xie *et al* using neon (where good quasihydrostatic conditions to at least 50 GPa can be offered [11]) suggests that the effect of non-hydrostaticity can be very limited. As a consequence, it appears that the abrupt stiffening of the *a*- and *c*-axes observed above 36 GPa in WB_4–Mn solid solutions is a second-order phase transition, which is similar to the *c*-axis softening observed at ~39 GPa in pure WB_4.

To gain a more direct insight into the structural change caused by the addition of Mn, we compare the variation of the *c*/*a* ratios between pure WB_4 and WB_4–Mn solid solutions. Figure 4(b) shows that the samples all show a linear increase in the *c*/*a* ratio up to ~36 GPa. Then, the *c*/*a* ratio demonstrates a sudden drop at ~39 GPa for WB_4 that is caused completely by *c*-axis softening, consistent with the observation at ~42 GPa by Xie *et al* [10, 11]. Although a more dramatic decrease in the *c*/*a* ratio is also demonstrated at a slightly lower pressure of ~36 GPa in $W_{0.96}Mn_{0.04}B_4$, this transition, associated by the suppression of *c*-axis softening observed in pure WB_4, is dictated by an abrupt *a*-axis stiffening. In addition, with the increase of Mn concentration to 16 at. % Mn (i.e. $W_{0.84}Mn_{0.16}B_4$), no significant changes in the *c*/*a* ratio are observed over the entire pressure range up to 52 GPa, which *h* can be accounted for by the simultaneous stiffening of the *a*- and *c*-axes at ~36 GPa. Similarly, we note that the $W_{0.93}Ta_{0.02}Cr_{0.05}B_4$ alloy also did not exhibit any drastic change in the *c*/*a* ratio; while the *c*-axis softening observed in pure WB_4 was suppressed, this process was accompanied by a smooth decrease for both *a*- and *c*-axes [17]. Thus, it is important to understand the origins of those anomalous lattice behaviors in WB_4–Mn solid solutions and to determine its correlation to the unique bonding structure in WB_4.

At ambient conditions, the WB_4 crystal lattice has recently be resolved to consist of alternating hexagonal layers of W and B atoms with some W-deficient sites filled randomly by boron trimers, which can couple with the B layers to produce slightly distorted cuboctahedral boron cages [9]. For the *c*-axis softening in pure WB_4, Xie *et al* excluded the probability of electronic topological transitions or Lifshitz transitions, and ascribed it to a reversible second-order phase transition that requires structural rearrangements and bond optimizing to accommodate high compression [11]. Besides, our latest high-pressure x-ray absorption spectroscopy study on WB_4 revealed that this transition can be initiated by the W-B bond weakening due to W 5*d* electron depletion. For $W_{0.93}Ta_{0.02}Cr_{0.05}B_4$, Mohammadi *et al* also proposed that the suppression of *c*-axis softening observed in pure WB_4 as well as the swap of the most compressible direction could stem from an electronic structure change with fundamentally altered bonding in the material [17]. Those results strongly suggest that in $W_{0.96}Mn_{0.04}B_4$ the suppression of *c*-axis softening should also be dominated by electronic structure effect, i.e. maximized W–B or B–B bond covalency of the rigid cage-like boron structure along the *c* direction arising from optimized VEC. In the meanwhile, because Mn has a much smaller atomic radius than W, the additional *a*-axis stiffening in $W_{0.96}Mn_{0.04}B_4$ should be attributed to atomic size effects that can influence available slip systems in *a*-*b* plane. However, as the Mn concentration increases, Xie *et al* [18] proposed that while the size mismatch effect should be improved, the optimal VEC might be exceeded, thus leading to a lower differential strain. Accordingly, the high hardness observed for the 10.0 at. % Mn sample (supporting information table 1) was attributed to dispersion hardening arising from the appearance of a second phase of MnB_4. However, the results of Mohammadi *et al* showed that MnB_4 starts to show up as an impurity phase only at and above 20 at. % Mn addition [17]. Also, we did not observe the presence of MnB_4 in the sample of $W_{0.84}Mn_{0.16}B_4$, thus excluding the possibility of an extrinsic effect. Moreover, our high-pressure result shows that when a higher concentration of Mn (16.0 at. %) is used, the *c*-axis actually becomes somewhat much stiffer than pure WB_4, suggesting the preservation of optimized VEC. This behavior might be due to the fact that adding Mn can not only increase VEC but also induce changes either in W vacancies or in the spatial distribution of boron cages, which can in turn optimize the VEC. Due to the bulk modulus' dependency on the spatially averaged VEC, the ~5% increase in the bulk modulus of $W_{0.84}Mn_{0.16}B_4$ relative to the pristine WB_4 (table 1) can be caused by the increased VEC. Moreover, the *a*-axis stiffening in $W_{0.84}Mn_{0.16}B_4$ shows a much larger magnitude than that in $W_{0.96}Mn_{0.04}B_4$, which is also compatible with the enhanced size mismatch effect. Therefore, these results suggest that the nearly identical hardness values in these

two solid solutions of $W_{0.96}Mn_{0.04}B_4$ and $W_{0.84}Mn_{0.16}B_4$ can originate from the combined intrinsic effects of atomic size mismatch and electronic structure change, and the latter may manifest itself as a dynamic optimization of VEC with Mn concentrations that is associated with modification of tungsten vacancies and boron trimers distribution in the 3D boron network of WB_4.

5. Conclusions

In summary, we have employed high-pressure XRD to explore the lattice compressibility of WB_4–Mn solid solutions up to 52 GPa. We find that the low and high Mn-doped WB_4 alloys (i.e. $W_{0.96}Mn_{0.04}B_4$ and $W_{0.84}Mn_{0.16}B_4$) are respectively more and less compressible than pure WB_4 under initial compression. Then, a lattice softening is shown to occur in the *c* direction above 39 GPa in pure WB_4, consistent with previous results. However, upon the addition of 4.0 at. % Mn to WB_4, it is surprising that an abrupt *a*-axis stiffening along with suppression of the *c*-axis softening observed in pure WB_4 is revealed at ~36 GPa. Moreover, when a higher concentration of Mn (16.0 at. %) is used, a simultaneous stiffening of the *a*- and *c*-axes is demonstrated at ~36 GPa. Without the presence of second phase, these results suggest that the nearly identical hardness values in these two solid solutions can originate from the combined intrinsic effects of atomic size mismatch and electronic structure change, which can manifest itself as a dynamic optimization of VEC with Mn concentration that is associated with a modification of tungsten vacancies and boron trimers distribution in the 3D boron network of WB_4. Our findings emphasize the importance of the best optimization and manipulation of the bonding and structure via solute atoms to the rational design of novel WB_4-based materials with enhanced mechanical properties.

Acknowledgments

This work is financially supported by the National Natural Science Foundation of China (Grants No. 11605225, 11475212 and 11505211), Youth Innovation Promotion Association CAS, and Jialin Xie Fundation of Institute of High Energy Physics, CAS.

ORCID iDs

Juncai Dong https://orcid.org/0000-0001-8860-093X
Zhiying Guo https://orcid.org/0000-0001-5904-3409

References

[1] Akopov G, Yeung M T and Kaner R B 2017 *Adv. Mater.* **29** 1604506
[2] Levine J B, Tolbert S H and Kaner R B 2009 *Adv. Funct. Mater.* **19** 3519
[3] Kaner R B, Gilman J J and Tolbert S H 2005 *Science* **308** 1268
[4] Li Q, Zhou D, Zheng W, Ma Y and Chen C 2015 *Phys. Rev. Lett.* **115** 185502
[5] Yeung M T, Mohammadi R and Kaner R B 2016 *Ann. Rev. Mater. Res.* **46** 2
[6] Turner C L, Zujovic Z, Koumoulis D, Taylor R E and Kaner R B 2019 *J. Mater. Sci.* **54** 3547
[7] Elizabeth M C *et al* 2018 *Supercond. Sci. Technol.* **31** 115005
[8] Pangilinan L E *et al* 2018 *Inorg. Chem.* **57** 15305
[9] Lech A T, Turner C L, Mohammadi R, Tolbert S H and Kaner R B 2015 *Proc. Natl Acad. Sci.* **112** 3223
[10] Xie M *et al* 2014 *Phys. Rev.* B **90** 104104
[11] Xie M *et al* 2012 *Phys. Rev.* B **85** 064118
[12] Mohammadi R *et al* 2011 *Proc. Natl Acad. Sci.* **108** 10958
[13] Akopov G *et al* 2018 *Chem. Mater.* **30** 3559
[14] Akopov G *et al* 2017 *J. Am. Chem. Soc.* **139** 17120
[15] Mohammadi R *et al* 2016 *Chem. Mater.* **28** 632
[16] Akopov G, Yeung M T, Turner C L, Mohammadi R and Kaner R B 2016 *J. Am. Chem. Soc.* **138** 5714
[17] Mohammadi R *et al* 2012 *J. Am. Chem. Soc.* **134** 20660
[18] Xie M *et al* 2015 *Appl. Phys. Lett.* **107** 041903
[19] Chung H-Y, Weinberger M B, Yang J-M, Tolbert S H and Kaner R B 2008 *Appl. Phys. Lett.* **92** 261904
[20] Xiong L *et al* 2015 *J. Alloys Compd.* **621** 116
[21] Xiong L *et al* 2013 *J. Appl. Phys.* **113** 033507
[22] Liu C *et al* 2011 *High Pressure Res.* **31** 275
[23] Gu Q, Krauss G and Steurer W 2008 *Adv. Mater.* **20** 3620
[24] Tao Q *et al* 2014 *Chem. Mater.* **26** 5297
[25] Hammersley A P, Svensson S O, Hanfland M, Fitch A N and Hausermann D 1996 *High Pressure Res.* **14** 235
[26] Toby B H 2001 *J. Appl. Crystallogr.* **34** 210
[27] Romans P A and Krug M P 1966 *Acta Crystallogr.* **20** 313
[28] Weinberger M B *et al* 2009 *Chem. Mater.* **21** 1915
[29] Niu H *et al* 2014 *Phys. Chem. Chem. Phys.* **16** 15866
[30] Gou H *et al* 2014 *Phys. Rev.* B **89** 064108
[31] Wang Z, Zhao Y, Schiferl D, Zha C S and Downs R T 2004 *Appl. Phys. Lett.* **85** 124
[32] Klotz S, Chervin J C, Munsch P and Le Marchand G 2009 *J. Phys. D: Appl. Phys.* **42** 075413